

1 Front. Chem. Sci. Eng.

2 DOI 10.1007/s11705-017-****-*

3 RESEARCH ARTICLE

4 Pyrolysis Transformation of ZIF-8 Wrapped with 5 Polytriazine to Nitrogen Enriched Core-shell Polyhedrons 6 Carbon for Supercapacitor

7 Nuoya Wang¹, Xinhua Huang(✉)¹, Lei Zhang¹, Jinsong Hu², Yimin Chao³, Ruikun Zhao(✉)⁴

8 1 School of Materials Science and Engineering, Anhui University of Science and Technology, Huainan,
9 Anhui, 232001, P. R. China

10 2 School of Chemical Engineering, Anhui University of Science and Technology, Huainan, Anhui,
11 232001, P. R. China

12 3 School of Chemistry, University of East Anglia, Norwich, NR4 7TJ, UK

13 4 College of Arts and Sciences, Khalifa University of Science and Technology, PO Box 127788, Abu
14 Dhabi, UAE

15 © Higher Education Press and Springer-Verlag GmbH Germany 2017

16 Received MM DD, 2017; accepted MM DD, 2017

17 E-mail: xhhuang@aust.edu.cn, ruikun.zhao@ku.ac.ae

18 **Abstract** This work presents a simple effective strategy to synthesize N-doped and shell-controlled
19 carbon nanocages through a package baking approach. A green approach to synthesize core-shell
20 ZIF-8@PTZ nanoparticles involves zinc contained ZIF-8 core wrapped by a N-enriched polytriazine
21 (PTZ). Synthesized core-shell ZIF-8@PTZ nanoparticles are calcinated to further sublime zinc through
22 PTZ shell and washed by HCl, leaving a porous carbon structure. At the meantime, hollow cavities were
23 introduced into N-doped carbon polyhedrons via the sacrifice of ZIF-8 template (noted as
24 ZIF-8@C/N-x). The electrochemical performance of the ZIF-8@C/N-x as supercapacitor electrode has
25 demonstrated high energy density and specific capacitance, as well as a long-term cycleability showing
26 92% capacitance retention after 10,000 cycles. There is a systematic correlation between
27 micro-/meso-porosity of ZIF-8@C/N-x and their electrochemical performances.

28 **Keywords** Core-shell, EDLC electrode, Microporos •Nano polygons, Nitrogen doped carbon

29 1 Introduction

30 Supercapacitors, are the most potential energy storage devices for lithium battery substituent alternatives,
31 owing to their high-power densities and fast charge-discharge performances [1-4]. It has been proved in
32 practice that carbon nanomaterials are the best choice as the supercapacitor electrode [5-7]. Carbon-based

33 materials inherit many natural features, such as excellent stability; high conductivity; economy-friendly
34 and ease to synthesis, which have been widely used for many energy supply implements [8-10].
35 Generally speaking, the electrochemical performances of carbon materials are determined by the
36 synergies of their specific surface areas, pore distributions, and the heteroatoms doped [11, 12]. Various
37 carbon-based nanomaterials for the applications in supercapacitors have been developed in the past
38 decades [13-15].

39 Metal organic frameworks (MOFs) are often used as the precursors that sacrifice later for preparing
40 porous carbon framework as a result of their high surface areas and adjustable pore structures [16-18].
41 Furthermore, N-enriched MOFs yields N-doped porous carbon can increase their carbon materials'
42 hydrophilicities and conductivities beneficial for their electrochemistry performance [19-21]. However,
43 the direct high-temperature carbonization of MOFs could collapse the regular structure and decrease the
44 surface areas although the N atoms are to be released easily during the pyrolysis. It is therefore necessary
45 to preserve the structures with N atom containing molecules [22-24]. For example, Zhang et al. using
46 Prussian-blue as the core and functionalized with N (or P)-doped carbon demonstrated high performance
47 in electrocatalysis [25,26]. Cheng et al. reported ZnO@MOF@PANI core-shell nanoarrays on carbon
48 cloth for high-performance supercapacitor electrodes [27]. Apparently, it has been evidenced that using
49 second carbon source on modified MOFs can enable the tuning of the structure and enhance the
50 electrochemical performance.

51 Zinc involving MOFs, specifically the zeolitic imidazolate framework (ZIF-8), could be simply
52 prepared with an accessible experiment in water at ambient temperature. Afterwards, zinc can be
53 sublimed from the mold and results in N-containing carbon material to form micropores. In literature,
54 ZIF-8-poly(cyclotriphosphazene-hexahydroxytriphenylene) [28], ZIF-8@CTAB [29], ZIF-8@PVP [30],
55 ZIF-8/urea [31] and ZIF-8@GO [32] are employed to produce the nitrogen-doped hierarchically porous
56 carbon at a high temperature. However, the complex preparation processes of carbon MOFs limit the
57 mass production with serious environmental pollutions. The preparation of electrodes from carbon
58 nanomaterials for supercapacitors should be easy and environment-friendly, and most importantly the
59 performance should meet the needs [33,34].

60 This study presents an approach of using N-enriched polytriazine (PTZ) as the second carbon source to
61 wrap ZIF-8, which through the package baking to synthesize porous and high N-doped carbon nanocages.
62 During carbonization in the high-temperature, the zinc sublimation produces pores in the obtained carbon
63 matrix, while the PTZ shell is transformed to N coexisted carbon nano- polyhedrons with cavities, which
64 are resulted from the sacrificial ZIF-8 template. A series of samples with different PTZ shell thicknesses
65 have been synthesized by the formation of the core-shell ZIF-8@C/N-x nano- polyhedrons and
66 pyrolyzation at high temperature. The electrochemical performances of supercapacitors using
67 ZIF-8@C/N-x electrodes have shown an explicit dependency on degree of N-doping and microporosity.
68 As a result, we have fabricated an electric double-layer capacitors electrode and demonstrated high
69 specific capacitance, power & energy densities, as well as long-term cycling stability.

70

71 2 Experimental

72 2.1 Materials preparations

73 All chemicals were acquired from Alfa Aesar and directly applied in the experiments. The detailed
74 synthesis processes are as follows:

75 **Synthesis of ZIF-8** in aqueous solution: The synthesis of ZIF-8 refers to the synthesis method in
76 literature [35]. 0.744 g of $Zn(NO_3)_2 \cdot 6H_2O$ was dissolved in 10 mL of deionized water, and 12.3 g of
77 dimethylimidazole was dissolved in 90 mL of deionized water. Then, the two solutions were mixed by
78 stirring for 24 h at ambient temperature. The ZIF-8 solution was prepared with a concentration of 4 mg
79 mL^{-1} .

80 **ZIF-8@PTZ**: 10 mL, 20 mL, and 30 mL ZIF-8 solutions were prepared in three 1 L glass cups
81 respectively, and distilled water was added to reach the volumes all to 600 mL exactly. Then
82 2,6-diaminopyridine (300 mg) and formaldehyde (450 μL) were added under vigorous stirring for 18 h at
83 room temperature. The crude samples were collected after centrifuge and washed with deionized water
84 and methanol, purified in a Soxhlet extractor for 48 h, followed by drying at 80 °C to obtain powder
85 samples.

86 **ZIF-8@C/N-x**: Under N_2 atmosphere, the dried samples were placed in tube furnace at 600 °C for 5 h,
87 then at 915 °C for 1 h to obtained the zinc contained sample. The sample was soaked in 3 M HCl
88 overnight to remove zinc, then rinsed repeatedly with deionized water before dried at 80 °C to obtained
89 the ZIF-8@C/N-x: x is the sample serial number, representing adding 10 mL, 20 mL, and 30 mL of
90 ZIF-8 solutions, respectively. The samples were named based on the amount of ZIF-8 during the
91 synthesis process, as ZIF-8@C/N-1, ZIF-8@C/N-2, ZIF-8@C/N-3.

92 2.2 Electrochemical measurement

93 A two-electrode system test was performed using an electrochemical workstation (CHI 760E, CH
94 Instrument, Shanghai) in 6 M KOH electrolyte. The sample, acetylene black, and PVDF were mixed in
95 NMP at a mass ratio of 8: 1: 1 to form a slurry and coated on nickel foam. Nickel foam was continued for
96 1 minute under a pressure of 10 MPa, then dried at 80 °C to make an electrode. The mass of the active
97 material on one electrode was about 1 to 2 mg, and the mass difference between the two electrodes does
98 not exceed 0.2 mg. The calculation on the single electrode mass ratio capacitance was based on the
99 galvanostatic charge/discharge (GCD) test. The calculation formula is given as below:

$$C=4(I \Delta t)/(m \Delta U) \quad (1)$$

100 The gravimetric energy density of the device E (Wh kg^{-1}) and P (W kg^{-1}) was calculated with the
101 equation below:

$$E=1/2 C \Delta U^2 \quad (2)$$

$$P=3600 E/\Delta t \quad (3)$$

102 Where I is the constant current in a constant current charge-discharge curve, m is the total mass of the
103 electrode, Δt is the discharge time, and ΔU is the discharge voltage.

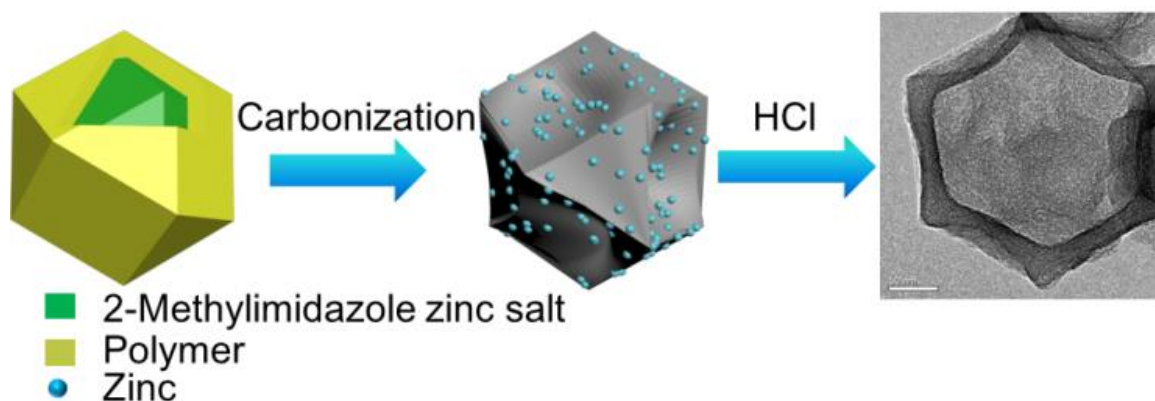
104 2.3 Materials characterizations

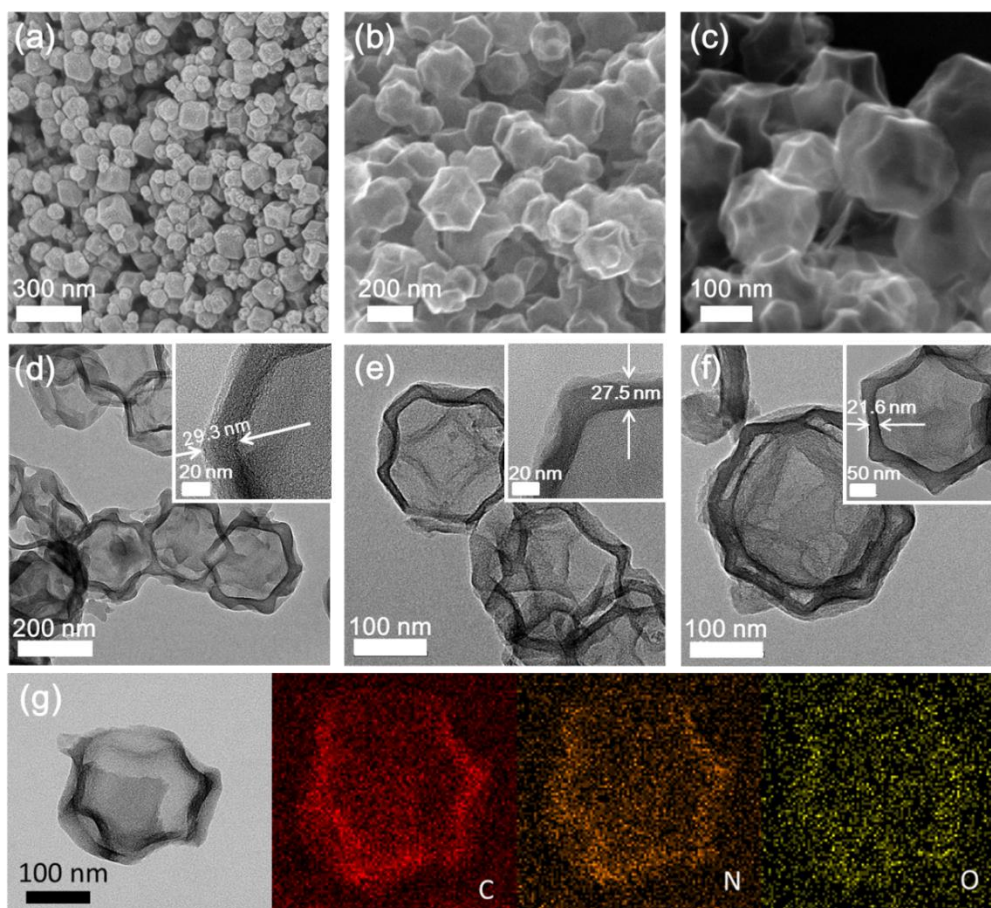
105 Scanning electron microscope (SEM) and transmission electron microscope (TEM) analysis were carried
106 out with a JEOL JEM-2100F instrument and JEOL, 1400 PLUS instrument respectively. X-ray
107 diffraction (XRD) measurements were conducted by X-ray diffractometer (Smartlab SE, Rigaku Ltd.,
108 Japan) with Cu radiation ($\lambda = 0.154$ nm). Raman spectroscopy was measured at room temperature with
109 Renishaw Invia RM200 (UK), under the condition of $\lambda_{\text{exc}} = 514$ nm, laser excitation was performed at
110 exposure time and excitation power of 10 s and 20 mW, respectively. Nitrogen (77 K) sorption isotherms
111 were measured from relative pressure P/P_0 of 6.9×10^{-8} to 0.992 using a Micromeritics ASAP 2020
112 analyzer. The conventional Brunauer-Emmett-Teller (BET) method and density functional theory (DFT)
113 method showed the specific surface area and pore size distributions.

114

115 3 Results and discussion

116 **Scheme 1** shows the schematic diagram of the synthetic route of ZIF-8@C/N-x. At room temperature,
117 formaldehyde and 2,6-diaminopyridine were polymerized in a dispersed ZIF-8 aqueous solution for 18 h
118 to form a PTZ. The ZIF-8 nanoparticles functioned as the core before being wrapped in a PTZ shell, then
119 the system was baked at a temperature of 915 °C to have the zinc sublimed at 907 °C under N₂
120 atmosphere [28]. ZIF-8 is in high nitrogen mass percentage, which can be conserved in the skeleton
121 framework of the porous carbon pro-carbonization [36]. As well known, N-doped carbon as energy
122 storage devices can enhance the conductivity, wettability with aqueous electrolyte and
123 pseudo-capacitance [19]. However, N in the ZIF-8 unavoidably lost during the carbonization processes at
124 high temperature. According to the recent literatures [37], PTZ has been employed as the secondary N
125 sources to prevent the N loss and protect the framework of ZIF-8, in addition to improving the
126 electrochemical performance, which can be easily synthesized in water at room temperature the same as
127 ZIF-8. During the process of annealing, Zn²⁺ from the core of the ZIF-8 polyhedrons converted to
128 metallic zinc by reduction reaction before subliming to the surface of PTZ shell, leaving
129 micro-/meso-porosity into the PTZ shell. At the end of annealing, the PTZ shell is modified to carbon
130 retaining hollow polygons with cavity generated from core ZIF-8 polyhedrons. The carbonized sample
131 was soaked in 3 M HCl overnight to remove remaining Zn in the sample, and finally polygonal porous
132 carbon ZIF-8@C/N-x were obtained.



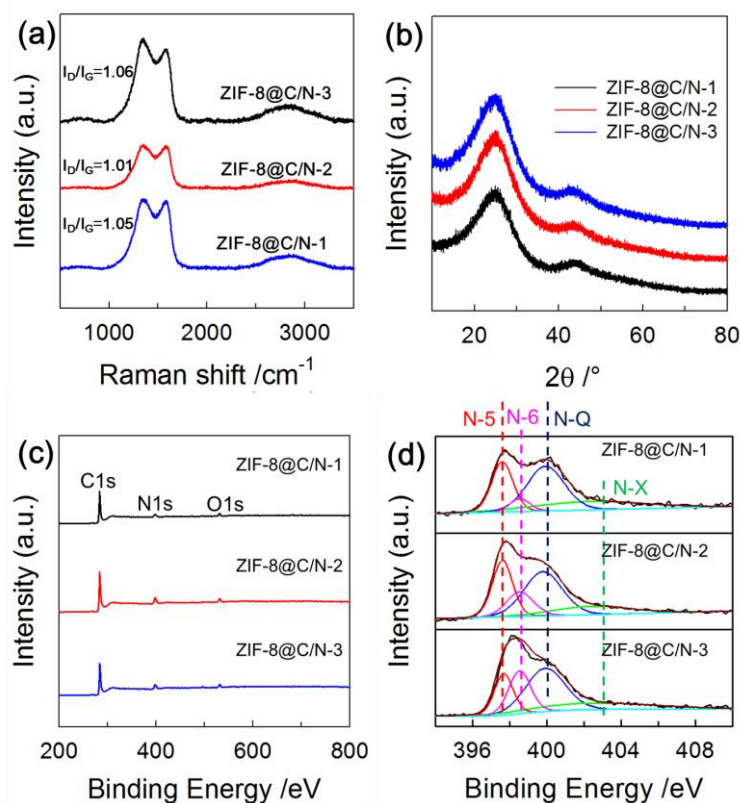


143

144 **Fig. 1** SEM images of (a) ZIF-8@C/N-1, (b) ZIF-8@C/N-2 and (c) ZIF-8@C/N-3; TEM images of (d) ZIF-8@C/N-1,
 145 (e) ZIF-8@C/N-2 and (f) ZIF-8@C/N-3 and the inset is the shell of C/N from corresponding PTZ. (g) The TEM images of
 146 ZIF-8@C/N-2 with element EDS mapping for C, N, O

147 The Raman spectrum in Fig. 2a shows the I_D/I_G band intensity ratios of ZIF-8@C/N-x. The G (1580
 148 cm^{-1}) peak arises from the vibrational mode of sp^2 bonded graphite carbon [36-38], while the D (1345
 149 cm^{-1}) band in the ZIF-8@C/N-x carbon becomes the prominent feature of the Raman spectrum [39], the
 150 high I_D/I_G (> 1) band intensity ratio of the ZIF-8@C/N-x is attributed for nitrogen doping [40] from the
 151 carbon precursors, which is beneficial for the charge transfer in the adsorption process [41].

152 XRD spectrum further characterizes the structure of ZIF-8@C/N-x. As shown in Fig. 2b, two broad
 153 diffraction peaks appeared at $\sim 23^\circ$ (2θ) and $\sim 42^\circ$ (2θ). The two reflections associated with the (002) and
 154 (100) planes of graphite indicates the dominant features in amorphous carbon [42]. There are no
 155 characteristic peaks of zinc in XRD spectrum, and combined with XPS analysis (Fig. 2c), it was found
 156 that most of the Zn in the sample has been removed, which does not have much impact on subsequent
 157 characterization.



158

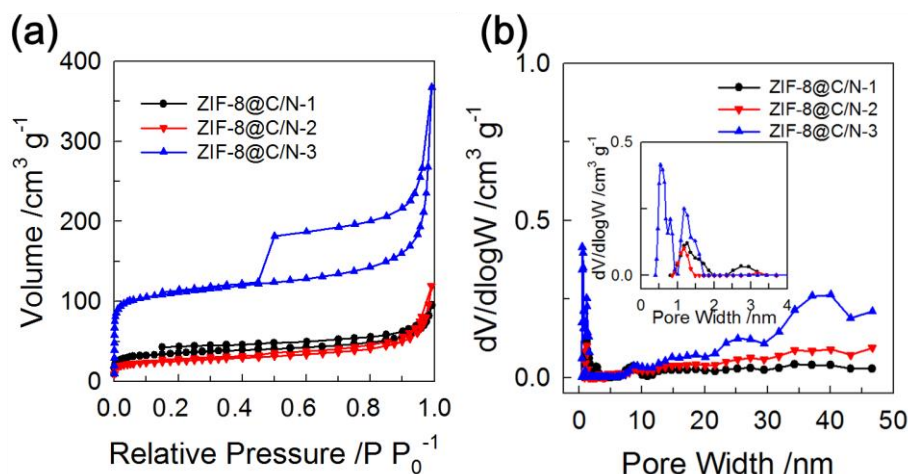
159 **Fig. 2** (a) Raman spectra and (b) XRD patterns of the ZIF-8@C/N-x samples, (c) XPS and (d) high-resolution XPS
 160 spectra of N1s the ZIF-8@C/N-x samples

161 The full XPS spectrum further evidenced the C, N, and O in ZIF-8@C/N-x samples. **Table 1** shows the
 162 percentage of N atoms based on the XPS data (wide scan in **Fig. 2c**). When the ZIF-8 increased during
 163 the preparation process, the atomic percentage of N also increased, which suggests that the imidazole
 164 component in the ZIF-8 template provided a part of N for the sample [28], meanwhile, the external C/N
 165 shell provided by PTZ does offset the nitrogen loss of the ZIF-8 during the carbonization. Pyridinic
 166 nitrogen (N-6), pyrrolic nitrogen (N-5), graphitic nitrogen (N-Q), and chemisorbed nitrogen oxides (N-X)
 167 are shown in the high-resolution N1s spectrum, corresponding to 397.6 eV, 398.5 eV, 399.9 eV and
 168 402.4 eV in the spectrum (**Fig. 2d**), respectively. Frankly speaking, the N-5 and N-6 are with
 169 characteristics of electron donors with high charge mobility, which could behave as active
 170 electrochemical active sites to capacitance increasing. On the other hand, the N-Q also improves the
 171 carbon material's conductivity by performing as electron donors and/or protons attractors, which could
 172 stimulate the redox reaction and enhance the rate performances [42-45]. The total content of N-5, N-6,
 173 N-Q in the N atoms of the sample is above 80%, which improves the specific capacitance of the sample.
 174 At the meantime, the presence of O atoms in the sample also provides a pseudo-capacitance to the
 175 sample and enhances the surface electrode's invasiveness [46-48].

176 **Table 1** Nitrogen composition of ZIF-8@C/N-x

Sample	N /wt%	N-6 /wt%	N-5 /wt%	N-Q /wt%	N-X /wt%
ZIF-8@C/N-1	19.57	27.34	6.61	42.39	23.66
ZIF-8@C/N-2	21.76	27.72	15.98	40.68	15.62
ZIF-8@C/N-3	22.24	18.42	22.44	40.08	19.06

177 The pore characteristics of all samples were analyzed by a N₂ adsorption-desorption (Fig. 3a).
 178 ZIF-8@C/N-1, 2 display type I sorption isotherms generated from microporous solids having relatively
 179 small external surfaces (e.g. molecular sieve zeolites, activated carbons, COFs/MOFs and certain porous
 180 oxides), while ZIF-8@C/N-3 displays a type IV sorption isotherm with type H4 hysteresis loop resulting
 181 from the mesopores [49,50]. The structural feature as mentioned above is further supported by the pore
 182 size distribution curves (Fig. 3b) and the averaged pore size was found to be 8.1-12.6 nm among the
 183 three ZIF-8@C/N-x samples (Table 2). The narrower pore size distribution of ZIF-8@C/N-x, the larger
 184 percentage of microporous surface area which is over 58% (e.g., 80% micropores of ZIF-8@C/N-3),
 185 ascribed to the Zinc sublimation and the PTZ after carbonization produced [50].



186
 187 **Fig. 3** (a) N₂ adsorption-desorption isotherms and (b) pore size distribution of ZIF-8@C/N-x

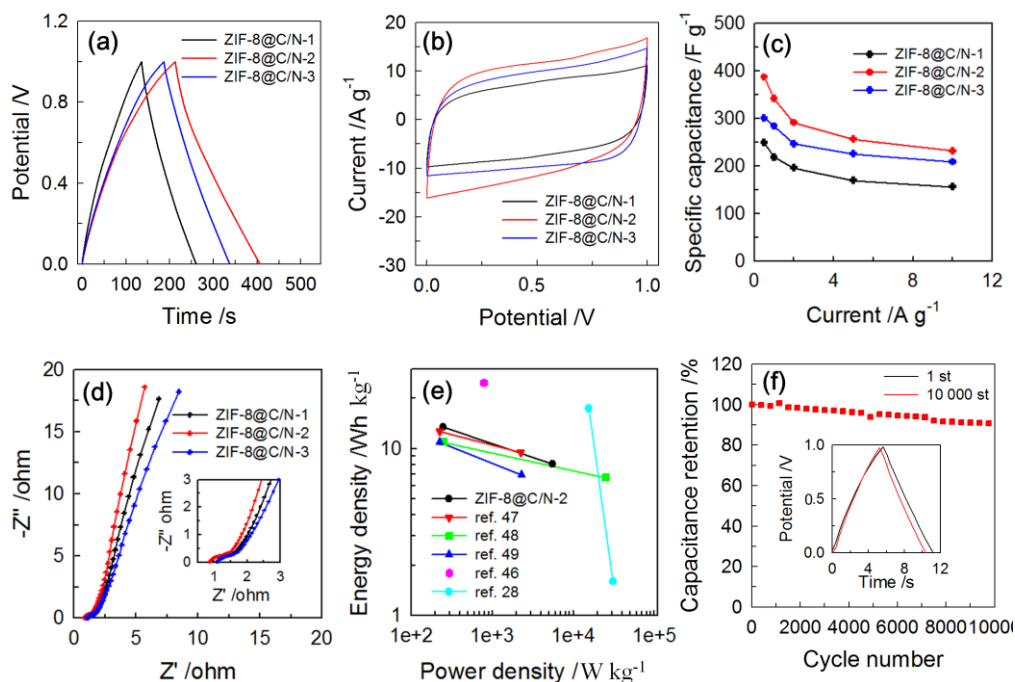
188 **Table 2** Porosity data of ZIF-8@C/N-x

Sample	S _{BET} ^{a)} /m ² g ⁻¹	Pore volume /cm ³ g ⁻¹	S _{micro} ^{b)} /m ² g ⁻¹	S _{meso} ^{c)} /m ² g ⁻¹	% _{micro} ^{d)}	Pore size /nm
ZIF-8@C/N-1	133	0.148	101.9	31.1	76	12.6
ZIF-8@C/N-2	93.9	0.185	54.6	39.3	58	14.8
ZIF-8@C/N-3	423.3	0.57	340	83.3	80	8.1

189 a) S_{BET}: specific surface area; b) S_{micro}: micropore surface area; c) S_{meso}: mesopore surface area; d) %_{micro}: the
 190 S_{micro} percent in the S_{BET}.

191 Fig. 4a presents the galvanostatic charge/discharge (GCD) curves with a current density of 0.5 A g⁻¹ of
 192 ZIF-8@C/N-x, as well as the GCD curves at various current densities are shown in Fig. S1a, c and e. The
 193 curve of ZIF-8@C/N-x slightly deviates from the linear shape which shows the presence of
 194 pseudo-capacitance [51]. Besides, ZIF-8@C/N-2 shows a much longer charge/discharge time than other
 195 samples, suggesting a higher specific capacitance value. This result suggests that more surfaces in
 196 ZIF-8@C/N-2 become accessible for electrolyte ions [52]. Fig. 4b shows the CV curves of ZIF-8@C/N
 197 electrodes at a scan rate of 200 mV s⁻¹ in 6 M KOH. All curves display a quasi-rectangular shape,
 198 indicating the synergistic contribution is from electric double-layer and faradaic capacitances. The CV
 199 curves were deformed which is mainly due to a surface redox reaction happened in the N-5 and N-6
 200 carbon matrix [53]. Additionally, the CV curve area of ZIF-8@C/N-2 is larger than other samples, which
 201 is consistent with the GCD results, indicating the highest capacitive property due to the highest N-5 and
 202 N-6 content from ZIF-8@C/N-2 (Table1) even though it quite poor porosities. The CV curves at various
 203 scan rates are shown in Fig. S1b, d and f, and the rectangular-like shape is maintained even swept at 500

204 mV s^{-1} , reflecting its excellent rate performances. The specific capacitance of the single electrode
205 calculated from the GCD curves at different current densities (Table. S1) is shown in Fig. 4c, and the
206 specific capacitance decreases with increasing current density. The Nyquist plots of ZIF-8@C/N-x are
207 presented in Fig. 4d. The EIS analysis is a common method to study the conductivity and the charge
208 transfer behaviors for electrode materials [54]. All the samples pointed low R_s values, suggesting that all
209 ZIF-8@C/N-x samples had low intrinsic resistances and charge transfer resistances. As can be seen from
210 the inset in Fig. 4d, ZIF-8@C/N-2 has lower intrinsic resistances and charge transfer resistances
211 compared to other samples. The inset of Fig. 4d shows the enlarged view of high frequency region and
212 equivalent circuit diagram. The high frequency intercept along the x-axis represents the equivalent series
213 resistance (R_s), a combination of the ionic resistance of the electrolyte, the intrinsic resistance of the
214 electrode material and interface resistance of the active material/current collector. The R_s of 1.11, 0.87
215 and 1.08 Ω for ZIF-8@C/N-1, 2 and 3, respectively, are observed from the intercept at the real axis. The
216 semicircle in the high frequency region stands for the interfacial charge-transfer resistance (R_{ct}) between
217 the electrode and electrolyte. The R_{ct} value for ZIF-8@C/N-2 was 0.31 Ω , which was lower than that of
218 pure ZIF-8@C/N-1 (0.62 Ω) and ZIF-8@C/N-3 (0.71 Ω). In the lower frequency region, all Nyquist
219 plots displayed a nearly vertically straight line, demonstrating the low ion diffusion/transport resistance
220 or the Warburg element (W). Fig. 4e shows the Ragone plots of ZIF-8@C/N-2 based on the specific
221 capacitances in the two-electrode system. Apparently, there is a minor decrease occurred in energy
222 density of the electrode material with increasing the power density for both carbons. The energy density
223 decreased from 13.43 Wh kg^{-1} to 8.05 Wh kg^{-1} as power density increased from 250 W kg^{-1} (0.5 A g^{-1})
224 to 5576.73 W kg^{-1} (10 A g^{-1}), implying that the decrease of the energy density is not really significant.
225 This is similar to most carbon materials [37,55-58]. In Table S2, the electrochemical performance of
226 ZIF-8@C/N-2 is compared with the N-C materials reported in the past two years. It can be seen
227 intuitively that ZIF-8@C/N-2 material has certain advantages compared with other materials, its energy
228 density is higher than most N-C materials and has a higher specific capacitance. Ragone plots of all the
229 four types of ZIF-8@C/N-x based electrodes are shown in Fig. S2. In addition, the cycle life of the
230 ZIF-8@C/N-2 electrodes is tested. Typically (Fig. 4f), after charge and discharge for 10,000 cycles at a
231 current density of 10 A g^{-1} , the ZIF-8@C/N-2 electrode retains 92% of the initial capacitance and the
232 charge-discharge curves maintain a triangular shape.



233
 234 **Fig. 4** (a) GCD curves and (b) CV curves of the as-prepared samples at a current density of 0.5 A g^{-1} and at a scan rate of
 235 200 mV s^{-1} ; (c) specific capacitances of the as-prepared samples at different current densities and (d) EIS of the
 236 as-prepared samples at the open circuit potential in the frequency range from 0.1 to 10^5 Hz . (e) Ragone plot (energy
 237 density vs. power density) of ZIF-8@C/N-2, another report's data are added for comparison, and (f) cyclic stability
 238 (current density of 10 A g^{-1})

239 4 Conclusions

240 In summary, the solid ZIF-8 nanoparticles have been wrapped in a nitrogen-containing PTZ to create a
 241 core-shell structure with different shell thicknesses. As a result, the core-shell ZIF-8@C/N-x
 242 nanoparticles were carbonized to ZIF-8@PTZ in high temperatures, shell thickness can be rational
 243 adjusted based on the ratio of wrapped PTZ. The porosity of derived PTZ could be precisely controlled
 244 by varying thicknesses of the shell due to its affection on zinc sublimation in the ZIF-8 core. The N%
 245 percentage in C/N shell was significantly affected by the preservation of the N releasing from ZIF-8 and
 246 its self-carbonization. The application of ZIF-8@C/N-x in super capacitor electrodes shows that the
 247 micro- and meso-pores of ZIF-8@C/N-x are playing vital role in the electrochemical performance. The
 248 highest specific capacitance of ZIF-8@C/N-2 (386.8 F g^{-1} at current density of 0.5 A g^{-1}) has been
 249 accomplished at an average diameter of 14.8 nm and 58% of micropore percentage. The ZIF-8@C/N-x in
 250 symmetric super-capacitors has shown significant high capacitance, high power and energy densities, as
 251 well as long-term capacitance cycling durability (92% retention at $10,000$ cycles). This green approach
 252 for synthesizing core-shell N-doped carbon nanomaterials provides a great potential for future materials
 253 in electrochemical applications such as electro-catalysts, Li-ion batteries, super-capacitors.

254 **Acknowledgements** This work was supported by the Key Project of Natural Science Research in
 255 Anhui Colleges and Universities (KJ2017A070), Anhui Province Natural Science Foundation Project
 256 (1908085ME157), and Anhui Province Selective Foundation of Innovation Project for Study Abroad
 257 (2019LCX020).

258 **Electronic Supplementary Material** Supplementary material is available in the online version of this
259 article at [http://dx.doi.org/\[DOI\]](http://dx.doi.org/[DOI]) and is accessible for authorized users.

260 **References**

- 261 1. Muzaffar A, Ahamed M B, Deshmukh K, Thirumalai J. A review on recent advances in hybrid supercapacitors: Design,
262 fabrication and applications. *Renewable & Sustainable Energy Reviews*, 2019, 101: 123–145
- 263 2. Sharma K, Arora A, Tripathi S K. Review of supercapacitors: Materials and devices. *Journal of Energy Storage*, 2019, 21:
264 801-825
- 265 3. Lu X F, Wang A L, Xu H, He X J, Tong Y X, Li G R. High-performance supercapacitors based on MnO₂ tube-in-tube
266 arrays. *Journal of Materials Chemistry A*, 2015, 3(32): 16560-16566
- 267 4. Xu H, Zhang C, Zhou W, Li G R. Co(OH)₂/RGO/NiO sandwich-structured nanotube arrays with special surface and
268 synergistic effects as high-performance positive electrodes for asymmetric supercapacitors. *Nanoscale*, 2015, 7(40): 16932-16942
- 269 5. Faraji S, Ani F N. The development supercapacitor from activated carbon by electroless plating-a review. *Renewable &*
270 *Sustainable Energy Reviews*, 2015, 42: 823-834
- 271 6. Li X, Wei B. Supercapacitor based on nanostructure carbon. *Nano Energy*, 2013, 2: 159-173
- 272 7. Zhang L L, Zhao X S. Carbon-based materials as supercapacitor electrodes. *Chemical Society Reviews*, 2009, 38(9):
273 2520-2531
- 274 8. Lu X F, Li G R, Tong Y X. A review of negative electrode materials for electrochemical supercapacitors. *Science*
275 *China-Technological Sciences*, 2015, 58(11): 1799-1808
- 276 9. Wang T, Li H G, Shi S J, Liu T, Yang G, Chao Y M, Yin F. 2D film of carbon nanofibers elastically astricted MnO
277 microparticles: a flexible binder-free anode for highly reversible lithium ion storage. *Small*, 2017, 13(20): 1604182
- 278 10. Chen L, Yan B, Xu J, Wang C G, Chao Y M, Jiang X F, Yang G. Bicontinuous structure of Li₃V₂(PO₄)₃ clustered via
279 carbon nanofiber as high-performance cathode material of Li-ion batteries. *ACS Applied Materials Interfaces*, 2015, 7(25):
280 13934-13943
- 281 11. Wang L, Chen L, Yan B, Wang C G, Zhu F, Jiang X F, Chao Y M, Yang G. In situ preparation of SnO₂@polyaniline
282 nanocomposites and their synergetic structure for high-performance supercapacitors. *Journal of Materials Chemistry A*, 2014,
283 2(22): 8334-8341
- 284 12. Ji H M, Ma C, Ding J J, Yang J, Yang G, Chao Y M, Yang Y. Complementary stabilization by core/sheath carbon
285 nanofibers/spongy carbon on submicron tin oxide particles as anode for lithium-ion batteries. *Journal of Power Sources*, 2019,
286 413: 42-49
- 287 13. Wang Q, Yan J, Fan Z. Carbon materials for high volumetric performance supercapacitors: design, progress, challenges and
288 opportunities. *Energy & Environmental Science*, 2016, 9(3): 729-762
- 289 14. Chen X, Paul R, Dai L. Carbon-based supercapacitors for efficient energy storage. *National Science Review*, 2017, 4(3):
290 453-489
- 291 15. Huang J S, Sumpter B G, Meunier V. Theoretical model for nanoporous carbon supercapacitors. *Angewandte Chemie*
292 *International Edition*, 2008, 47(3): 520-524
- 293 16. Yang S J, Kim T, Im J H, Kim Y S, Lee K, Jung H, Park C R. MOF-derived hierarchically porous carbon with exceptional
294 porosity and hydrogen storage capacity. *Chemistry of Materials*, 2012, 24(3): 464-470

- 295 17. Chaikittisilp W, Ariga K, Yamauchi Y. A new family of carbon materials: synthesis of MOF-derived nanoporous carbons
296 and their promising applications. *Journal of Materials Chemistry. A*, 2013, 1(1): 14-19
- 297 18. Ren Q, Wang H, Lu F X, Gong Y X, Li G R. Recent progress on MOF-derived heteroatom-doped carbon-based
298 electrocatalysts for oxygen reduction reaction. *Advanced Science*, 2017, 5(3): 1700515
- 299 19. Li W H, Hu S H, Luo X Y, Li Z L, Sun X Z, Li M S, Liu F F, Yu Y. Confined amorphous red phosphorus in MOF-derived
300 N-doped microporous carbon as a superior anode for sodium-ion battery. *Advanced Materials*, 2017, 29(16): 1605820
- 301 20. Chai L L, Zhang L J, Wang X, Xu L Q, Han C, Li T T, Hu Y, Qian J J, Huang S M. Bottom-up synthesis of MOF-derived
302 hollow N-doped carbon materials for enhanced ORR performance. *Carbon*, 2019, 146: 248-256
- 303 21. Ren Q, Wang H, Lu X F, Tong Y X, Li G R. Recent progress on MOF-derived heteroatom-doped carbon-based
304 electrocatalysts for oxygen reduction reaction. *Advanced Science*, 2018, 5(3): 1700515
- 305 22. Liu Y, Miao W, Fang X, Tang Y L, Wu D L, Mao S. MOF-derived metal-free N-doped porous carbon mediated
306 peroxydisulfate activation via radical and non-radical pathways: Role of graphitic N and C-O. *Chemical Engineering Journal*,
307 2020, 380: 122584
- 308 23. Yang H X, Zhao D L, Meng W J, Zhao M, Duan Y J, Han X Y, Tian X M. Nickel nanoparticles incorporated into N-doped
309 porous carbon derived from N-containing nickel-MOF for high-performance supercapacitors. *Journal of Alloys & Compounds*,
310 2019, 782: 905-914
- 311 24. Zhao L Y, Yu J, Xing C T, Ullah Z, Yu C C, Zhu S P, Chen M L, Li W W, Li Q, Liu L W. Nanopore confined
312 anthraquinone in MOF-derived N-doped microporous carbon as stable organic cathode for lithium-ion battery. *Energy Storage*
313 *Materials*, 2019, 22: 433-440
- 314 25. Zhang L, Hu J S, Huang X H, Song J, Lu S Y. Particle-in-box nanostructured materials created via spatially confined
315 pyrolysis as high performance bifunctional catalysts for electrochemical overall water splitting. *Nano Energy*, 2018, 48: 489-499
- 316 26. Lv C N, Zhang L, Huang X H, Zhu Y X, Zhang X, Hu J S, Lu S Y. Double functionalization of N-doped carbon carved
317 hollow nanocubes with mixed metal phosphides as efficient bifunctional catalysts for electrochemical overall water splitting.
318 *Nano Energy*, 2019, 65: 103995
- 319 27. Zhu C M, He Y, Liu Y J, Kazantseva N, Saha P, Cheng Q L. ZnO@MOF@PANI core-shell nanoarrays on carbon cloth for
320 high-performance supercapacitor electrodes. *Journal of Energy Chemistry*, 2019, 35: 124-131
- 321 28. Kale V S, Hwang M, Chang H, Kang J, Chae S I, Jeon Y, Yang J, Kim J, Ko Y J, Piao Y, Hyeon T.
322 Microporosity-controlled synthesis of heteroatom codoped carbon nanocages by wrap-bake-sublime approach for flexible
323 all-solid-state-supercapacitors. *Advanced Functional Materials*, 2018, 28(37): 1803786
- 324 29. Jiang M, Cao X P, Zhu D D, Duan Y X, Zhang J M. Hierarchically porous N-doped carbon derived from ZIF-8
325 nanocomposites for electrochemical applications. *Electrochimica Acta* 2016, 196: 699-707
- 326 30. Lai Q X, Zhao Y X, Liang Y Y, He J P, Chen J H. In situ confinement pyrolysis transformation of ZIF-8 to
327 nitrogen-enriched meso-microporous carbon frameworks for oxygen reduction. *Advanced Functional Materials*, 2016, 26(45):
328 8334-8344
- 329 31. Ma X C, Li L Q, Zeng Z, Chen R F, Wang C H, Zhou K, Su C Q, Li H L. Synthesis of nitrogen-rich nanoporous carbon
330 materials with C₃N-type from ZIF-8 for methanol adsorption. *Chemical Engineering Journal*, 2019, 363: 49-56
- 331 32. Ding B, Fan Z J, Lin Q Y, Wang J, Chang Z, Li T, Henzie J, Kim J, Dou H, Zhang X G, Yamauchi Y. Confined pyrolysis
332 of ZIF-8 polyhedrons wrapped with graphene oxide nanosheets to prepare 3D porous carbon heterostructures. *Small Methods*,
333 2019, 3(11): 1900277

- 334 33. Chen Y Z, Wang C M, Wu Z Y, Xiong Y J, Xu Q, Yu S H, Jiang H L. From bimetallic metal-organic framework to porous
335 carbon: high surface area and multicomponent active dopants for excellent electrocatalysis. *Advanced Materials*, 2015, 27(34):
336 5010-5016
- 337 34. Feng J X, Ye S H, Wang A L, Lu X F, Tong Y X, Li G R. Flexible cellulose paper-based asymmetrical thin film
338 supercapacitors with high-performance for electrochemical energy storage. *Advanced Functional Materials*, 2014, 24(45):
339 7093-7101
- 340 35. Tanaka S, Kida K, Okita M, Ito Y, Miyake Y. Size-controlled synthesis of zeolitic imidazolate framework-8 (ZIF-8)
341 crystals in an aqueous system at room temperature. *Chemistry Letters*, 2012, 41(10): 1337-1339
- 342 36. Ferrari A C, Robertson J. Interpretation of Raman spectra of disordered and amorphous carbon. *Physical Review B*, 2000,
343 61(20): 14095-14107
- 344 37. Huang X H, Wang N Y, Li F, Zhu X X, Liao K, Chan V, Zhang L. Molecular engineering of supercapacitor electrodes with
345 monodispersed N-doped carbon nanoporous spheres. *New Journal of Chemistry*, 2019, 43(40): 15892-15898
- 346 38. Zhu J, Kong L R, Shen X P, Chen Q R, Ji Z Y, Wang J H, Xu K Q, Zhu G X. Three-dimensional N-doped
347 graphene/polyaniline composite foam for high performance supercapacitors. *Applied Surface Science* 2018, 428: 348-355
- 348 39. Zhang S, Sui L, Kang H Q, Dong H Z, Dong L F, Yu L Y. High performance of N-doped graphene with bubble-like
349 textures for supercapacitors. *Small*, 2018, 14(5): 1702570
- 350 40. Dai S G, Liu Z, Zhao B T, Zeng J H, Hu H, Zhang Q B, Chen D C, Qu C, Dang D, Liu M L. A high-performance
351 supercapacitor electrode based on N-doped porous graphene. *Journal of Power Sources*, 2018, 387: 43-48
- 352 41. Liu Y, Pan L K, Chen T Q, Xu X T, Lu T, Sun Z, Chua D H C. Porous carbon spheres via microwave-assisted synthesis for
353 capacitive deionization. *Electrochimica Acta*, 2015, 151: 489-496
- 354 42. Zou K X, Deng Y F, Chen J P, Qian Y Q, Yang Y W, Li Y W, Chen G H. Hierarchically porous nitrogen-doped carbon
355 derived from the activation of agriculture waste by potassium hydroxide and urea for high-performance supercapacitors. *Journal*
356 *of Power Sources*, 2018, 378: 579-588
- 357 43. Liu T Y, Zhang F, Song Y, Li Y. Revitalizing carbon supercapacitor electrodes with hierarchical porous structures. *Journal*
358 *of Materials Chemistry A*, 2017, 5(34): 17705-17733
- 359 44. Ouyang T, Cheng K, Gao Y, Kong S, Ye K, Wang G, Cao D. Molten salt synthesis of nitrogen doped porous carbon: a new
360 preparation methodology for high-volumetric capacitance electrode materials. *Journal of Materials Chemistry A*, 2016, 4(25):
361 9832-9843
- 362 45. Wang D W, Li F, Yin L C, Lu X, Chen Z G, Gentle I R, Qing (max) Lu G, Cheng H M. Nitrogen-doped carbon monolith
363 for alkaline supercapacitors and understanding nitrogen - induced redox transitions. *Chemistry – A European Journal*, 2012,
364 18(17): 5345-5351
- 365 46. Song Z Y, Zhu D Z, Xue D F, Yan J J, Chai X L, Xiong W, Wang Z W, Lv Y K, Cao T C, Liu M X, et al.,
366 Nitrogen-enriched hollow porous carbon nanospheres with tailored morphology and microstructure for all-solid-state symmetric
367 supercapacitors. *ACS Applied Energy Materials*, 2018, 1(8): 4293-4303
- 368 47. Zhao G Y, Chen C, Yu D F, Sun L, Yang C H, Zhang H, Sun Y, Besenbacher F, Yu M. One-step production of O-N-S
369 co-doped three-dimensional hierarchical porous carbons for high-performance supercapacitors. *Nano Energy*, 2018, 47: 547-555
- 370 48. Xue D F, Zhu D Z, Liu M X, Duan H, Li L C, Chai X L, Wang Z W, Lv Y K, Xiong W, Gan L H. Schiff-base/resin
371 copolymer under hypersaline condition to high-level N-doped porous carbon nanosheets for supercapacitors. *ACS Applied Nano*
372 *Materials*, 2018, 1(9): 4998-5007

- 373 49. Kim W, Joo J B, Kim N, Oh S, Kim P, Yi J. Preparation of nitrogen-doped mesoporous carbon nanopipes for the
374 electrochemical double layer capacitor. *Carbon*, 2009, 47(5): 1407-1411
- 375 50. Tang J, Liu J, Li C L, Li Y Q, Tade M O, Dai S, Yamauchi Y. Synthesis of nitrogen - doped mesoporous carbon spheres
376 with extra - large pores through assembly of diblock copolymer micelles. *Angewandte Chemie International Edition*, 2015, 54(2):
377 588-593
- 378 51. Gao F, Shao G H, Qu J Y, Lv S Y, Li Y Q, Wu M B. Tailoring of porous and nitrogen-rich carbons derived from hydrochar
379 for high-performance supercapacitor electrodes. *Electrochimica Acta*, 2015, 155: 201-208
- 380 52. Zhang X S, Yan P T, Zhang R J, Liu K, Liu Y Y, Liu T, Wang X Y. A novel approach of binary doping sulfur and nitrogen
381 into graphene layers for enhancing electrochemical performances of supercapacitors. *Journal of Materials Chemistry A*, 2016,
382 4(48): 19053-19059
- 383 53. Hou S J, Wang M, Xu X T, Li Y D, Li Y J, Lu T, Pan L K. Nitrogen-doped carbon spheres: A new high-energy-density and
384 long-life pseudo-capacitive electrode material for electrochemical flow capacitor. *Journal of Colloid & Interface Science*, 2017,
385 491: 161-166
- 386 54. Hulicova D, Yamashita J, Soneda Y, Hatori H, Kodama M. Supercapacitors prepared from melamine-based carbon.
387 *Chemistry of Materials*, 2005, 17(5): 1241-1247
- 388 55. Xin L J, Li R M, Lu Z T, Liu Q, Chen R R, Li J Q, Liu J Y, Wang J. Hierarchical metal-organic framework derived
389 nitrogen-doped porous carbon by controllable synthesis for high performance supercapacitors. *Journal of Electroanalytical
390 Chemistry*, 2018, 813: 200-207
- 391 56. Li X Q, Hao C L, Tang B C, Wang Y, Liu M, Wang Y W, Zhu Y H, Lu C G, Tang Z Y. Supercapacitor electrode materials
392 with hierarchically structured pores from carbonization of MWCNTs and ZIF-8 composites. *Nanoscale*, 2017, 9(6): 2178-2187
- 393 57. Chen L F, Lu Y, Yu L, Lou X W D. Designed formation of hollow particle-based nitrogen-doped carbon nanofibers for
394 high-performance supercapacitors. *Energy & Environmental Science*, 2017, 10(8): 1777-1783
- 395 58. Salunkhe R R, Kamachi Y, Torad N L, Hwang S M, Sun Z, Dou S X, Kim J H, Yamauchi Y. Fabrication of symmetric
396 supercapacitors based on MOF-derived nanoporous carbons. *Journal of Materials Chemistry. A*, 2014, 2(46): 19848-19854